



Retrieval of $O_2(^1\Sigma)$ and $O_2(^1\Delta)$ volume emission rates in the mesosphere and lower thermosphere using SCIAMACHY MLT limb scans

Amirmahdi Zarboo¹, Stefan Bender^{1,a}, John P. Burrows², Johannes Orphal¹, and Miriam Sinnhuber¹

¹Institute of Meteorology and Climate Research (IMK-ASF), Karlsruhe Institute of Technology, Karlsruhe, Germany

²Institute of Environmental Physics, University of Bremen, Bremen, Germany

^anow at: Department of Physics, Norwegian University of Science and Technology, Trondheim, Norway

Correspondence: Amirmahdi Zarboo (amirmahdi.zarboo@kit.edu)

Received: 27 July 2017 – Discussion started: 14 August 2017

Revised: 16 November 2017 – Accepted: 9 December 2017 – Published: 23 January 2018

Abstract. We present the retrieved volume emission rates (VERs) from the airglow of both the daytime and twilight $O_2(^1\Sigma)$ band and $O_2(^1\Delta)$ band emissions in the mesosphere and lower thermosphere (MLT). The SCanning Imaging Absorption SpectroMeter for Atmospheric CHartographY (SCIAMACHY) onboard the European Space Agency Envisat satellite observes upwelling radiances in limb-viewing geometry during its special MLT mode over the range 50–150 km. In this study we use the limb observations in the visible (595–811 nm) and near-infrared (1200–1360 nm) bands.

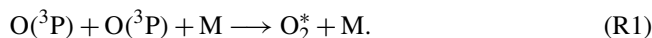
We have investigated the daily mean latitudinal distributions and the time series of the retrieved VER in the altitude range from 53 to 149 km. The maximal observed VERs of $O_2(^1\Delta)$ during daytime are typically 1 to 2 orders of magnitude larger than those of $O_2(^1\Sigma)$. The latter peaks at around 90 km, whereas the $O_2(^1\Delta)$ emissivity decreases with altitude, with the largest values at the lower edge of the observations (about 53 km). The VER values in the upper mesosphere (above 80 km) are found to depend on the position of the sun, with pronounced high values occurring during summer for $O_2(^1\Delta)$. $O_2(^1\Sigma)$ emissions show additional high values at polar latitudes during winter and spring. These additional high values are presumably related to the downwelling of atomic oxygen after large sudden stratospheric warmings (SSWs). Accurate measurements of the $O_2(^1\Sigma)$ and $O_2(^1\Delta)$ airglow, provided that the mechanism of their production is understood, yield valuable information about both the chemistry and dynamics in the MLT. For example, they can be

used to infer the amounts and distribution of ozone, solar heating rates, and temperature in the MLT.

1 Introduction

The atmospheric airglow in the mesosphere and thermosphere above ≈ 60 km is formed by fluorescent emission from excited states of atoms and molecules. Atoms and molecules in the mesosphere and lower thermosphere (MLT) can be excited by absorption of solar radiation (photoluminescence) or by exothermic chemical reactions (chemiluminescence; see, e.g., Brasseur and Solomon, 2006).

The processes that contribute to the airglow of atomic and molecular oxygen in the mesosphere and lower thermosphere are shown in Fig. 1. The recombination of atomic oxygen (Barth, 1964), denoted as Reaction (R1) and (*k*) in Fig. 1, produces O_2^* excited molecules:



Here, O_2^* represents any of the seven states below the first dissociation limit. Bates and others argue that the population distribution between these states can best be approximated statistically, in which the $^5\Pi_g$ state is produced in almost 40 % of the collisions (Smith, 1984; Bates, 1992; Wraight, 1982). Most of the O_2^* derived from recombination is found in the $A^3\Sigma_u^+$ state (Slanger and Copeland, 2003), and in a recent review Huestis concludes that all of the recombining atoms pass through the Herzberg states $c^1\Sigma_u^-$, $A'^3\Delta_u$, and

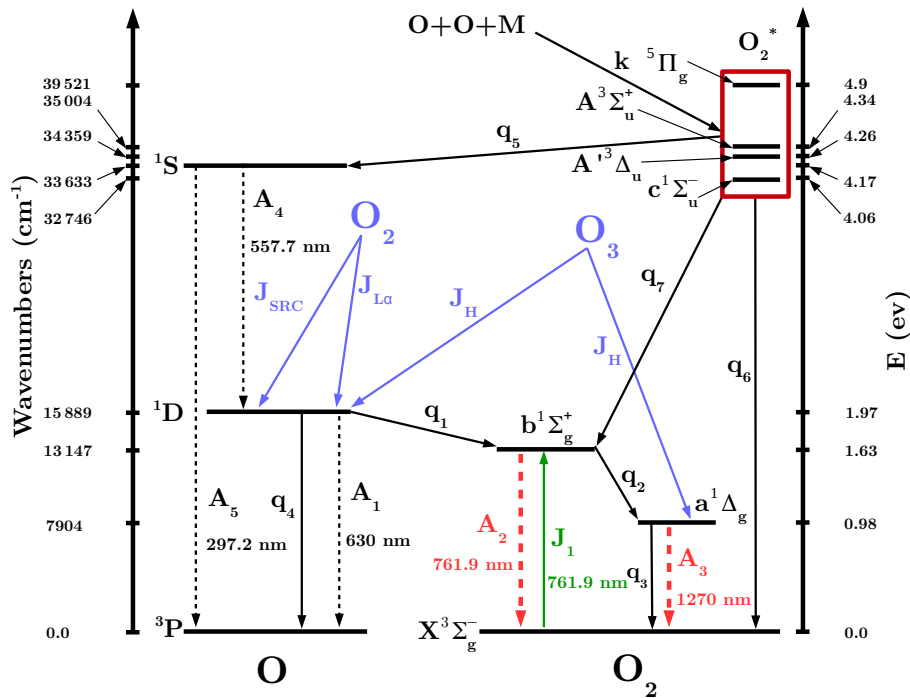


Figure 1. Schematic overview depicting processes that contribute to the production of Oxygen emission bands in the middle atmosphere. The black solid arrows are the most important gas phase reactions (k) and quenching reactions (q_i). The blue and green solid arrows are photodissociation and photoexcitation processes respectively (J_i). Dashed arrows correspond to spontaneous radiative emissions (A_i), and the red dashed arrows show the radiative emissions that are the subject of this study. (*) in O_2^* denotes several excited states (see text for explanation).

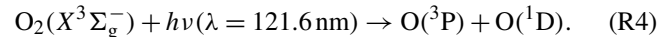
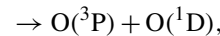
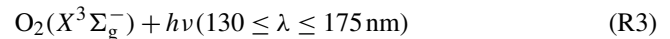
$A^3\Sigma_u^+$ (Huestis, 2013). Stegman and Murtagh (1991) provide the quenching parameters resulted from analyzing the measurements of the near-ultraviolet portion of the night-glow to fit the synthetic spectra of the Herzberg bands of O_2 . These parameters set an upper limit of 10% production efficiency on the generation of $O_2(c^1\Sigma_u^-)$ in the atomic oxygen association reaction. Admittedly, proper accounting of the correct products of Reaction (R1) can be complex. Recent research has investigated this issue (e.g., Kirillov, 2012, 2014). Therefore we assume the production of a surrogate “hybrid” state O_2^* in the photochemical model.

The photolysis of ozone (J_H in Fig. 1, Reaction R2) in the Hartley band ($\lambda < 310$ nm) leads to the first electronically excited state of atomic oxygen $O(^1D)$ and molecular oxygen $O_2(a^1\Delta_g)$ (DeMore, 1966):

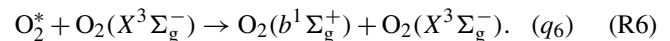
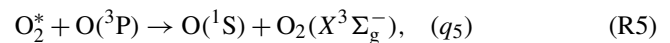


The photolysis of molecular oxygen in the Schumann–Runge continuum (J_{SRC} in Fig. 1, Reaction R3) and at Lyman α ($J_{L\alpha}$ in Fig. 1, Reaction R4) leads to electronically excited

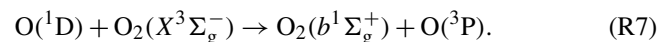
oxygen atoms $O(^1D)$ (Nicolet, 1971):



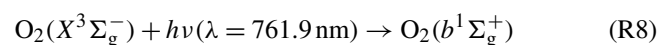
Quenching (collisional de-excitation) processes are represented by black solid arrows and denoted by (q_i) in Fig. 1. The O_2^* , produced by Reaction (R1), can be quenched by atomic oxygen to produce $O(^1S)$ via Reaction (R5) (q_5 in Fig. 1) (Barth and Hildebrandt, 1961) or quenched by molecular oxygen to produce $O_2(b^1\Sigma_g^+)$ via Reaction (R6) (q_6 in Fig. 1) (Greer et al., 1981):



$O(^1D)$, by quenching with $O_2(X^3\Sigma_g^-)$, produces $O_2(b^1\Sigma_g^+)$ via Reaction (R7), which combines q_1 and q_4 in Fig. 1 (Mlynczak and Olander, 1995):

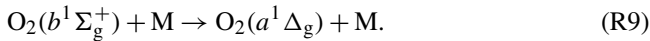


Photoabsorption of the solar radiation at 761.9 nm produces $O_2(b^1\Sigma_g^+)$ directly via



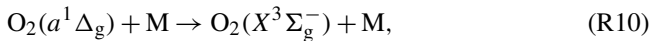
in the sunlit mesosphere (Mlynczak et al., 1993), shown in Fig. 1 as the radiative excitation J_1 .

Then, according to Reaction (R9), O₂($b^1\Sigma_g^+$) can be reduced in energy to O₂($a^1\Delta_g$) by collisions with any of the abundant species such as O₂, N₂, CO₂, or O (denoted by “M”), shown as q_2 in Fig. 1 (Mlynczak and Olander, 1995):



Note that the above is a fast process (spin-conserved).

O₂($a^1\Delta_g$) can in turn be quenched via Reaction (R10) (q_3 in Fig. 1) to produce O₂($X^3\Sigma_g^-$):

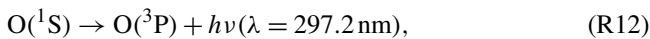


which is a slow process (spin forbidden because the ground state is O₂($X^3\Sigma_g^-$)).

Spontaneous radiative emissions are represented by dashed arrows and denoted by (A_i) in Fig. 1. O(¹S) decays to O(¹D) by emitting 557.7 nm photons (the oxygen green line, Reaction R11, A_4 in Fig. 1), which is fast (because it conserves the spin) (Barth and Hildebrandt, 1961):

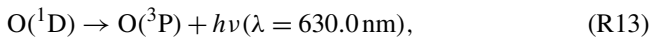


Reactions (R1), (R5), and (R11) are commonly referred to as the Barth mechanism (Barth and Hildebrandt, 1961; see, e.g., the review by Bates, 1981). The green line emission allows the deduction of the atomic oxygen densities near 100 km, as shown for example by Lednyts'kyy et al. (2015). The oxygen 297.2 nm line is one of the prominent components of the ultraviolet nightglow (Slanger et al., 2006), and it is produced by O(¹S) via Reaction (R12) (Khomich et al., 2008):



which is indicated by A_5 in Fig. 1.

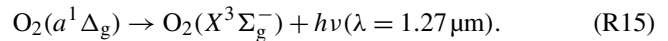
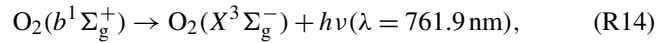
O(¹D) – produced from Reactions (R2, J_H), (R3, J_{SRC}), (R4, J_α), or (R11, A_4) – can be deactivated to the ground state O(³P) by the slow (spin-forbidden) emission:



where the 630.0 nm red line (Khomich et al., 2008) is represented by A_1 in Fig. 1.

Among the strongest features of the day and night airglow are the infrared atmospheric band ($a^1\Delta_g \rightarrow X^3\Sigma_g^-$) and the atmospheric band ($b^1\Sigma_g^+ \rightarrow X^3\Sigma_g^-$) of molecular oxygen (Wayne, 1994). These two spontaneous radiative emissions, which we deal with in this work, are represented by the thick red dashed arrows in Fig. 1. They are emitted by the deactivation of the two excited states of the molecular oxygen O₂($b^1\Sigma_g^+$) at 761.9 nm via Reaction (R14) (A_2 in Fig. 1) and O₂($a^1\Delta_g$) at 1.27 μm via Reaction (R15) (A_3 in Fig. 1)

(Mlynczak et al., 1993):



Assuming that the processes in Fig. 1 describe the photochemistry and chemistry, one can deduce ozone densities from measurements of the infrared atmospheric volume emission rates (VERs) in the O₂($b^1\Sigma_g^+$) and O₂($a^1\Delta_g$) bands (hereafter O₂(¹Σ) and O₂(¹Δ) bands respectively). For this, the rates of all of these processes such as q_1 and q_4 in Fig. 1 and in the Reactions (R7) and (R9) should be known (e.g., Evans et al., 1968; Thomas et al., 1983; Mlynczak and Olander, 1995; Mlynczak et al., 2001).

1.1 Previous measurements

The oxygen airglow was measured from spaceborne platforms and rocket experiments in several previous studies. Measurements of the O₂(¹Σ) band include the Fabry–Pérot interferometer on the Dynamics Explorer 2 (DE-2) satellite (Skinner and Hays, 1985), which were used to study the overall brightness of the emission. The high-resolution Doppler imager (HRDI) on the Upper Atmosphere Research Satellite (UARS) (Hays et al., 1993) measured the Doppler shifts of rotational lines of the O₂(¹Σ) atmospheric band to determine the winds in the stratosphere, mesosphere, and lower thermosphere. The Wind Imaging Interferometer (WINDII) on the same satellite (Shepherd et al., 1993) measured wind, temperature, and emission rates. The TIMED Doppler Interferometer (TIDI) on the Thermosphere–Ionosphere–Mesosphere Energetics and Dynamics (TIMED) satellite (Killeen et al., 2006) performed remote sensing measurements of upper atmosphere winds and temperatures based on O₂(¹Σ) emission. The Remote Atmospheric and Ionospheric Detection System (RAIDS) on the International Space Station’s Kibo module (Christensen et al., 2012) measured the limb brightness of the O₂(¹Σ) (0,0), (0,1), and (1,1) vibrational band emissions from 80 to 180 km. The Optical Spectrograph and InfraRed Imaging System (OSIRIS), onboard the Odin satellite (Sheese et al., 2010), was used to derive temperatures in the mesosphere and lower thermosphere region (MLT) from O₂(¹Σ).

Previous measurements of the O₂(¹Δ) band include observations from the near-infrared spectrometer experiment on the Solar Mesosphere Explorer satellite (SME). SME measured emission from O₂(¹Δ) produced by photolysis of O₃ (Thomas et al., 1984). The infrared atmospheric-band airglow radiometer (IRA) aboard the satellite OHZORA measured the mesospheric ozone profile derived from O₂(¹Δ) emission (Yamamoto et al., 1988). One part of the Optical Spectrograph and InfraRed Imager System instrument onboard the Odin satellite is a three-channel infrared imager (IRI) that observes the scattered sunlight and the airglow from the oxygen infrared atmospheric band at 1.27 μm

(Llewellyn et al., 2004). The TIMED–SABER (Sounding of the Atmosphere using Broadband Emission Radiometry) data were used to measure the $O_2(^1\Delta)$ airglow emission by a channel with central wavelength of 1.27 μm (Gao et al., 2011a).

All of the abovementioned studies include satellite observations of only one of the O_2 bands, either $O_2(^1\Sigma)$ or $O_2(^1\Delta)$. Simultaneous measurements of both $O_2(^1\Delta)$ and $O_2(^1\Sigma)$ airglow were part of the Mesosphere–Thermosphere Emissions for Ozone Remote Sensing (METEORS) sounding rocket experiment. It was launched from White Sands Missile Range, New Mexico (Mlynczak et al., 2001), and was used to derive ozone concentrations separately from each of the O_2 bands.

1.2 Present work

In this work, we retrieve volume emission rates from the airglow of the $O_2(^1\Sigma)$ and $O_2(^1\Delta)$ bands in the mesosphere and lower thermosphere from the SCanning Imaging Absorption SpectroMeter for Atmospheric CHartographY (SCIAMACHY Burrows et al., 1995, Bovensmann et al., 1999 and references therein) onboard the European Space Agency Envisat satellite. We present the retrieval algorithm and $O_2(^1\Sigma)$ and $O_2(^1\Delta)$ band volume emission rates. We analyze daily mean latitudinal distributions of VERs in the altitude range of approximately 50–150 km.

In Sect. 2 we describe the SCIAMACHY dataset and our method to retrieve both the $O_2(^1\Delta)$ and the $O_2(^1\Sigma)$ volume emission rates. Results are presented in Sect. 3, including the retrieved volume emission rates and first results on the temporal and spatial variations of the volume emission rates. We also include one example study of the relation between the temporal variations and the sudden stratospheric warming (SSW) in 2009. In Sect. 4 we summarize the findings of our study and give conclusions.

2 Data and methods

2.1 Data

The SCanning Imaging Absorption SpectroMeter for Atmospheric CHartographY is a passive remote sensing spectrometer that observes back-scattered, reflected, transmitted, or emitted radiation from the atmosphere and the Earth's surface in the 240–2380 nm wavelength range. The instrument is part of the atmospheric chemistry payload onboard the Envisat satellite, which was operational from March 2002 until April 2012. SCIAMACHY has three different viewing geometries: nadir, limb, and moon–sun occultations. From July 2008 until April 2012, SCIAMACHY observed the mesosphere and lower thermosphere region (50–150 km) regularly twice a month. This special MLT limb mode scans the mesosphere and lower thermosphere in 30 limb points from 50 to 150 km altitude with a vertical spacing of about 3 km. These

scans were scheduled in place of the nominal mode scans and there were 20 limb scans along one semi-orbit. Overall 84 days of mesosphere and lower thermosphere limb measurements were carried out. In this work, we use the visible and near-infrared spectra from channel 4 (595–811 nm) and channel 6 (1200–1360 nm) in the MLT limb-viewing geometry to retrieve volume emission rates (VERs) from the airglow of the $O_2(^1\Sigma)$ and $O_2(^1\Delta)$ bands. Use of the additional channels covering the green line or UV is beyond our current work, and we refer to Lednyts'kyy et al. (2015).

To generate data for our study, we used the SCIAMACHY dataset level 1b version 8.02 and the SCIAMACHY command line tool `SciaLlc`¹ from the SCIAMACHY calibration tools. We selected two windows for each of the two bands: 750–780 nm for the $O_2(^1\Sigma)$ band (759–767 nm) and 1200–1360 nm for the $O_2(^1\Delta)$ band (1255–1285 nm). We subtract the spectrum measured at ≈ 360 km tangent height as a dark spectrum from the measured spectra at all of the other tangent heights. This spectrum contains some residual spectral (readout) patterns left from the calibration step, and subtracting it from other spectra which have almost the same patterns cancels out that. For the $O_2(^1\Delta)$ band, there are two masked points that appear in every scan located around 1262 and 1282 nm.

2.2 Daytime spectra

A typical orbit starts with a limb measurement of the twilight atmosphere, followed by the solar occultation measurement during sunrise over the North Pole and an optimized limb-nadir sequence (Bovensmann et al., 1999). Our criterion to select daytime observations out of twilight measurements is that we require the tangent point solar zenith angle to be less than or equal to 88°. Using this approach we avoid twilight measurements and all of the measurement points are located on the dayside.

Examples of the daytime-calibrated spectra for orbit number 41 455, measured on 3 February 2010 at a mean latitude of 17.3° N and a mean longitude of 94.3° E, are shown in Fig. 2a for the $O_2(^1\Sigma)$ band and in Fig. 2b for the $O_2(^1\Delta)$ band.

The spectral region used to observe the daytime $O_2(^1\Sigma)$ spectrum includes a Rayleigh-scattering background which perturbs the retrieval. Consequently it is necessary to estimate the Rayleigh scattering and subtract it from the observational spectrum to yield the $O_2(^1\Sigma)$ emission spectra. This background scattering is attributed in part to the upwelling radiation, multiple scattering in the lower atmosphere, and the terrestrial albedo. This results in an absorption signature for $O_2(^1\Sigma)$ (Sheese et al., 2010). To account for the multiple scattering and absorption from the ground state $O_2(^3\Sigma_g)$ to the $O_2(^1\Sigma)$, a background signal comprising the $O_2(^1\Sigma)$

¹<https://earth.esa.int/web/guest/software-tools/content/-/article/socialc-command-line-tool-4073>

spectrum at the highest altitude (≈ 148 km) scaled to the ratio of the mean of the out-of-band radiances is subtracted from the limb spectra at each tangent height. We consider the spectra in the 750–759 and 767–780 nm as out of band.

After this correction, we subtract a linear background from the whole signal in each level. An example of the background-subtracted spectrum containing the O₂(¹Σ) emission is shown in Fig. 2c.

For the O₂(¹Δ) band, the absorption signature in the spectral background is negligible compared to the daytime O₂(¹Σ) band spectra; therefore, we only subtract a linear background from the observation. An example for the daytime O₂(¹Δ) band spectra with background subtracted is shown in Fig. 2d.

2.3 Twilight spectra

Because the tangent point solar zenith angle for the sun being below the horizon varies with tangent altitude, we use Eq. (1) to calculate the horizon angle for each tangent point (R is the radius of the Earth and h is the tangent point height):

$$\alpha_{\text{horizon}} = \frac{\pi}{2} + \cos^{-1} \left(\frac{R}{R+h} \right). \quad (1)$$

As a criterion to select twilight data, we remove every limb scan in which at least one point measurement has a solar zenith angle less than given by Eq. (1). Based on this, we obtain the O₂(¹Σ) and the O₂(¹Δ) background-subtracted twilight spectra shown in Fig. 3a and c for the example orbit (41 455). For the twilight O₂(¹Δ) band, we apply the same background subtraction as for daylight. Figure 3b shows the twilight O₂(¹Δ) spectra, and panel (d) shows the background-corrected twilight O₂(¹Δ) spectra for the same example orbit (41 455). It is apparent that the background signal is negligible for both of the O₂(¹Σ) and O₂(¹Δ) twilight spectra.

2.4 Retrieval

To invert the observed radiation to spectral emission rates, we set up 30 layers around the Earth, such that each layer is centered at one tangent height. We denote the observed spectral radiances by \mathbf{Y} , the path length of each of the observed lines of sight through each of the atmospheric layers by \mathbf{L} , and the emission rate from the layer by \mathbf{X} . Assuming no self-absorption, this yields the linear relation

$$\mathbf{Y} = \mathbf{LX}. \quad (2)$$

In Eq. (2), $\dim(\mathbf{Y}) = \text{number of atmospheric layers} \times \text{number of spectral points} = 30 \times 144$ for the O₂(¹Σ) band and 30×210 for the O₂(¹Δ) band. $\dim(\mathbf{L}) = \text{number of the atmospheric layers} \times \text{number of tangent heights in each scan} = 30 \times 30$. $\dim(\mathbf{X}) = \text{number of atmospheric layers} \times \text{number of spectral points in the corresponding wavelength interval} = 30 \times 144$ for O₂(¹Σ) and 30×210 for O₂(¹Δ).

We solve Eq. (2) by minimizing $\|\mathbf{Y} - \mathbf{LX}\|^2$ using standard least squares and normalization with the error covariance matrix \mathbf{S}_y and obtain the inverted spectral emission intensity \mathbf{X} :

$$\mathbf{X} = (\mathbf{L}^T \mathbf{S}_y^{-1} \mathbf{L})^{-1} \mathbf{L}^T \mathbf{S}_y^{-1} \mathbf{Y}. \quad (3)$$

The error covariance matrix \mathbf{S}_y has diagonal elements of the out-of-band variances of the background-corrected spectra in each altitude.

3 Results

3.1 Inverted spectra

Using our method in Sect. 2.4, the emission intensities are calculated for the spectra described in Sect. 2.2 and 2.3. Examples of the emission intensity for daytime O₂(¹Σ) are shown in Fig. 4a and for daytime O₂(¹Δ) in Fig. 4b.

The spectral shapes of the O₂(¹Σ) band in the daytime O₂(¹Σ) spectra and of the O₂(¹Δ) band in the daytime O₂(¹Δ) spectra are clearly visible. We find that the largest values for the daytime O₂(¹Σ) band are located at about 90 km altitude, and for the O₂(¹Δ) band at 54 km, noting that the SCIAMACHY MLT scan range is 50 to 150 km. We also note that the maximum O₂(¹Δ) emission intensities in each limb scan are about 2 orders of magnitude larger than the maximum values of the O₂(¹Σ) band in the corresponding limb scan.

Figure 4c shows the twilight O₂(¹Σ) emission intensity, and Fig. 4d shows the twilight O₂(¹Δ) emission intensity for the same orbit but retrieved from one of the three twilight MLT scans (see Sect. 2.3). The O₂(¹Σ) band is about 1 order of magnitude smaller than during daylight. The twilight O₂(¹Δ) band signal is more pronounced but about 2 orders of magnitude smaller than during the day. The error bars in the panels of Fig. 4 represent the square root of each of the diagonal elements of the retrieval error covariance matrix \mathbf{S}_a for each altitude:

$$\mathbf{S}_a = \mathbf{GS}_y \mathbf{G}^T, \quad (4)$$

in which the contribution function matrix \mathbf{G} is defined as

$$\mathbf{G} = (\mathbf{L}^T \mathbf{S}_y^{-1} \mathbf{L})^{-1} \mathbf{L}^T \mathbf{S}_y^{-1}. \quad (5)$$

Evaluating all altitudes, not shown here but indicated in Fig. 4a, we observe the strongest signal of daytime O₂(¹Σ) around 83–99 km. Hereafter, we use the term “significant” for data with a signal-to-noise ratio (SNR) greater than 1.

Figure 4c shows that the twilight O₂(¹Σ) band emission intensities have large noise masking the signal. The daytime O₂(¹Δ) emission intensities are in general of higher SNR than the twilight O₂(¹Δ) emission intensities. The daytime O₂(¹Δ) emission intensities are strongest at the lowest observable altitudes, i.e., 54 km (Fig. 4b). The strongest twilight O₂(¹Δ) emissions are located in the 83–96 km altitude range (Fig. 4d shows only a selection of altitudes).

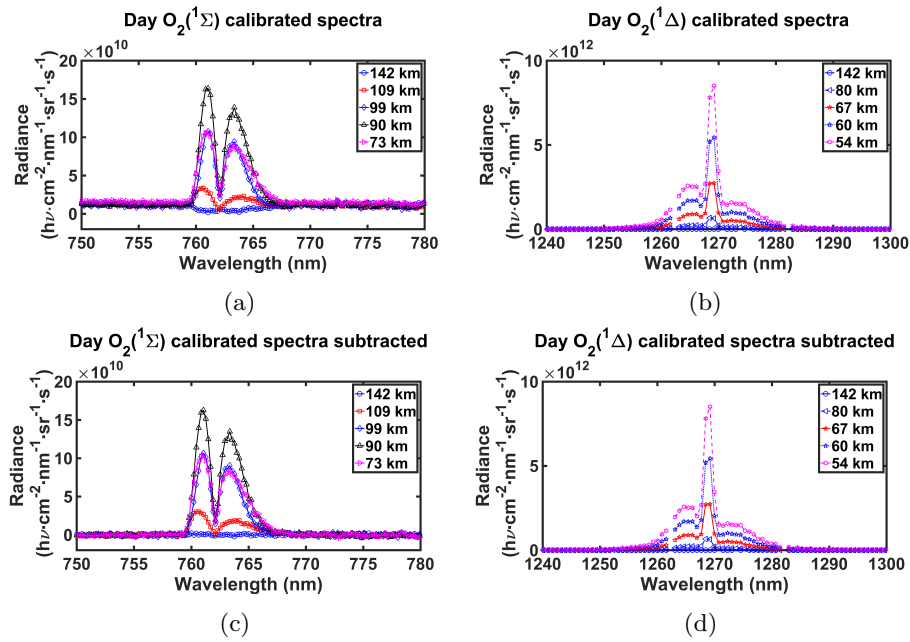


Figure 2. Examples of the daytime-calibrated spectra and the background-corrected spectra. (a) $O_2(^1\Sigma)$ on 3 February 2010; orbit 41 455; mean latitude 17.3° N, mean longitude 94.3° E. (b) as (a) but for the $O_2(^1\Delta)$ band. (c) as (a) but with background correction applied. (d) as (b) but with background correction applied.

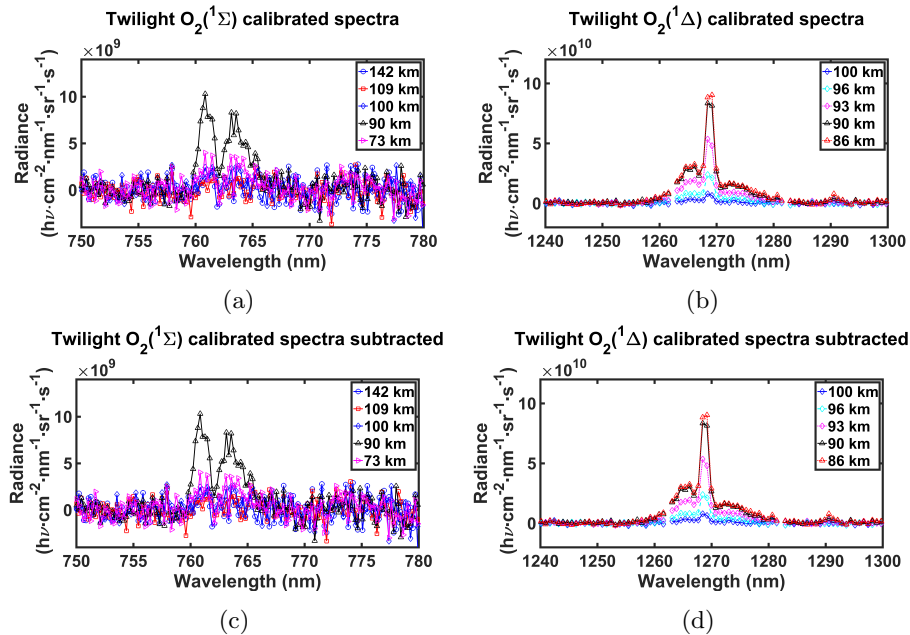


Figure 3. Examples of the twilight-calibrated spectra and the spectra from which the background $O_2(^3\Sigma_g^-)$ to $O_2(^1\Sigma)$ absorption has been subtracted. (a) for the $O_2(^1\Sigma)$ band on 3 February 2010; orbit number 41 455; mean latitude of 78.0° N, mean longitude of 226.5° E. (b) as (a) but for the $O_2(^1\Delta)$ band. (c) as (a) but with background subtracted. (d) as (b) but with background subtracted.

3.2 Volume emission rates

We integrate the spectral emission intensity from 759 to 767 nm to obtain the $O_2(^1\Sigma)$ band integrated volume emis-

sion rate. Volume emission rate profiles for one sample satellite orbit (41 455 on 3 February 2010) for daytime $O_2(^1\Sigma)$ and $O_2(^1\Delta)$ are shown in Fig. 5a and b respectively. Examples of the volume emission rate latitude–altitude distribu-

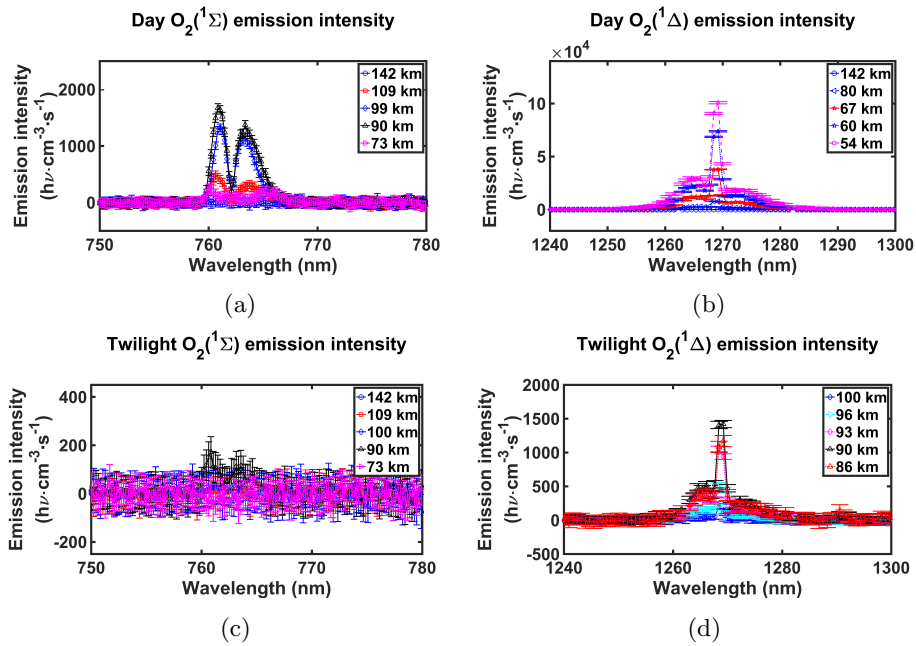


Figure 4. Examples of the emission intensities that are obtained by solving Eq. (3). (a) For the daytime $O_2(^1\Sigma)$ band on the date 3 February 2010; orbit number 41 455; mean latitude of 17.3° N, mean longitude of 94.3° E. (b) as (a) but for the $O_2(^1\Delta)$ band. (c) For the twilight $O_2(^1\Sigma)$ band on the date 3 February 2010; orbit number 41 455; mean latitude 78.0° N, mean longitude 226.5° E. (d) as (c) but for the $O_2(^1\Delta)$ band. Error bars represent the retrieval errors.

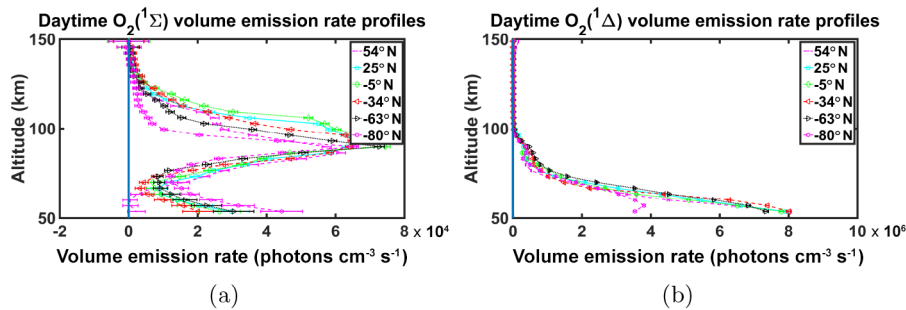


Figure 5. Typical profiles of the VER for different latitudes. (a) For the daytime $O_2(^1\Sigma)$ VER on the date 3 February 2010; orbit number 41 455. (b) as (a) for the daytime $O_2(^1\Delta)$ band. Error bars represent the retrieval errors.

tions for the same orbit for daytime $O_2(^1\Sigma)$ are shown in Fig. 6a and for daytime $O_2(^1\Delta)$ in Fig. 6b. The blank regions represent areas with signal-to-noise ratios of less than 1.

The $O_2(^1\Sigma)$ VER has its maximum in the 90–98 km altitude range, which is 2 orders of magnitude smaller than the $O_2(^1\Delta)$ maximum VER, as shown in Fig. 5a. The volume emission rate profile of dayglow $O_2(^1\Delta)$ observed by TIMED–SABER often has its maximum around 50 km altitude, as shown for example in Fig. 1 of Mlynczak et al. (2007). Figure 5b shows that the SCIAMACHY MLT volume emission rate profiles are largest at the bottom of the observed altitude range, around 54 km. These VER profiles sometimes show secondary maxima in the range 80–90 km, which are at least 1 order of magnitude smaller than the

largest SCIAMACHY VER. This secondary maximum occurs especially around equinox times. The measurement errors of the volume emission rates (not shown here) for different orbits show that the $O_2(^1\Sigma)$ volume emission rates are significant from 65 to 140 km and do not depend on latitude. Inspecting the volume emission rate altitude profiles (not shown here), we see that the $O_2(^1\Sigma)$ volume emission rates have the largest SNR below 125 km and above 85 km. The best signal of the $O_2(^1\Delta)$ VER is below 95 km.

In a region above the South Atlantic and off the Brazilian coast, the Earth’s magnetic field is anomalously low and the ionizing radiation can be increased by several orders of magnitude. This region is called the South Atlantic Anomaly (SAA, see for example Kurnosova et al., 1962) and any

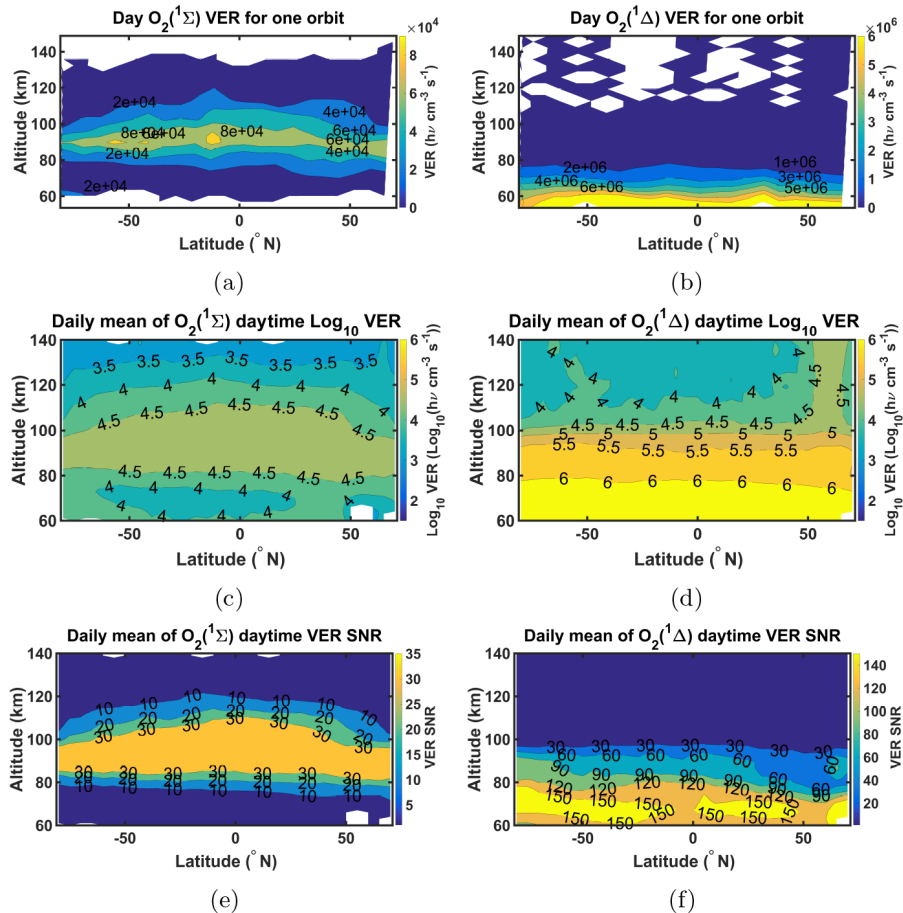


Figure 6. Latitude–altitude contours of the daytime VER. **(a)** for the $O_2(^1\Sigma)$ band and for one satellite orbit on the date 3 February 2010; orbit number 41 455. **(b)** as **(a)** for $O_2(^1\Delta)$. Signal-to-noise ratios less than 1 and large noisy values are excluded. **(c)** and **(d)** as **(a)** and **(b)** respectively, averaged on all of the orbits on the whole day of 3 February 2010, with the same logarithmic scale. Negative values are excluded. **(e)** Signal-to-noise ratios of the daily mean of $O_2(^1\Sigma)$ VERs. Areas where the signal-to-noise ratio is less than 1 are plotted in white. **(f)** as **(e)** for the $O_2(^1\Delta)$ band.

spacecraft which crosses this region can give false instrument readings. In our retrievals, the SNRs of the volume emission rates in the orbits that cross this region are affected by the SAA. The most dramatic influence of the SAA on our dataset is on the $O_2(^1\Sigma)$ volume emission rates SNR, although the values are still significant in the 80–100 km altitude range. The SAA influences the $O_2(^1\Sigma)$ measurements more than the $O_2(^1\Delta)$ measurements.

3.3 Daily mean VER latitude–altitude distributions

We calculate the daily mean VERs as follows. We bin the measurements into 5° latitude bins. In each bin, the measurements located within $\pm 2.5^{\circ}$ are attributed to that latitude and averaged to the daily mean VER. An example of the daily mean daytime $O_2(^1\Sigma)$ VER latitude–altitude distribution (on 3 February 2010) is shown in Fig. 6c and of the daily mean daytime $O_2(^1\Delta)$ VER in Fig. 6d (VERs with low signal-to-noise ratios and with large measurement errors

are excluded). The daily mean $O_2(^1\Sigma)$ VERs have maximum values of about 1–2 orders of magnitude smaller than $O_2(^1\Delta)$. Similar to our results for a single orbit (Sect. 3.2), we observe the largest $O_2(^1\Delta)$ VER below 60 km and the largest $O_2(^1\Sigma)$ VER at 90 km.

To assess the signal-to-noise ratio for the daytime VERs, Fig. 6e shows the daily mean $O_2(^1\Sigma)$ VER signal-to-noise ratios. We observe the strongest signal of daytime $O_2(^1\Sigma)$ in the 70–130 km altitude range. The strongest signal of the twilight $O_2(^1\Sigma)$ is observed between 84 and 95 km (not shown here). Figure 6f shows that the stronger signal of daytime $O_2(^1\Delta)$ is observed below 105 km, with the strongest around 70 km. The largest signal of twilight $O_2(^1\Delta)$ is observed in the altitude range of 83–97 km (not shown).

3.4 Time series

In the following, we discuss the variation of the daily mean VERs versus latitude and time. First we will discuss the tem-

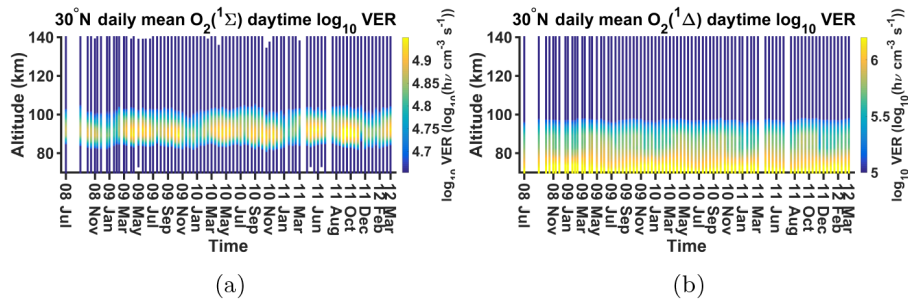


Figure 7. Time series of the daily mean VER. (a) for the daytime $O_2(^1\Sigma)$ VER; 30° N; July 2008 to March 2012. (b) as (a) for the daytime $O_2(^1\Delta)$ band.

poral variation in the mesosphere and lower thermosphere (70–140 km) at 30° N. Thereafter we will discuss the variation of the peak values, peak altitudes, and centroid altitudes as a function of time and latitude.

3.4.1 Time series at 30° N

By calculating the daily mean VERs for all of the days on which SCIAMACHY MLT limb scans are available, we obtain time series of the daily mean VERs from July 2008 to March 2012. An example of these time series of the daily mean daytime $O_2(^1\Sigma)$ VER, chosen for 30° N from all altitude combinations, is shown in Fig. 7a and for the daytime $O_2(^1\Delta)$ VER of the same location in Fig. 7b.

We found a semi-annual variation with the strongest $O_2(^1\Sigma)$ signal in the 90–95 km range during May–June and September–November and the lowest signal in December–March, with a secondary minimum in August. The highest values of the $O_2(^1\Delta)$ VER are located at the lowest altitude of observations, formed mostly by ozone photodissociation (Thomas et al., 1984). We observe secondary maximum values which mostly occur in May–June and September–November (approximately spring and autumn) in the 75–95 km altitude range. The secondary maximum of $O_2(^1\Delta)$ occurs in the same altitude range and with the same temporal variation as the $O_2(^1\Sigma)$ signal. This will be investigated in more detail in the following section.

3.4.2 Variation of peak values

Next we evaluate the variations of the maximal daily mean VERs in the mesosphere and lower thermosphere with respect to latitude and time. For this, we derive the maximal values from the daily mean VERs for $O_2(^1\Sigma)$ and between 85 and 100 km altitude for $O_2(^1\Delta)$, which are shown in Fig. 8a and b respectively. Only those regions are shown in Fig. 8b, d, and f where the secondary maxima of $O_2(^1\Delta)$ exist. The peak altitudes are also obtained at the same time and will be discussed in Sect. 3.4.3. The maxima of the $O_2(^1\Sigma)$ VER at middle to low latitudes (60° S– 60° N) appear to be correlated with the maximum intensity of solar radiance. Ad-

ditionally, we sometimes observe attenuations in the maximum values in the late northern winters, mostly from late January until early March of each year. Also there are some high values at northern polar latitudes: in spring 2009, from autumn to spring 2009–2010, from autumn to winter 2010, and from autumn to spring 2011–2012.

The secondary maxima of the $O_2(^1\Delta)$ VER are confined to winter at mid-to-high latitudes.

The correlation of the $O_2(^1\Sigma)$ VERs with the solar radiance suggests formation caused by solar light, either by ozone photolysis (Reactions R2 and R7) or by larger abundances of atomic oxygen owing to stronger O_2 photolysis. In the second case, the formation of the excited states could also be due to the recombination of atomic oxygen (Reactions R1 and R6). The maximal values at high latitudes, where the solar flux is low, in general suggest other sources such as recombination of atomic oxygen (Thomas et al., 1984). This is true in particular for $O_2(^1\Sigma)$, where high values occur at high latitudes in winter and spring; these are probably caused by downward transport of thermospheric atomic oxygen into the mesosphere and lower thermosphere.

There are two possibilities for secondary maxima of $O_2(^1\Delta)$. They happen in the region where the secondary ozone maximum is strongest. Also, atomic oxygen densities might be strongest due to enhanced mixing with the lower thermosphere. Detailed study of the processes which result in the formation of the secondary maxima of $O_2(^1\Delta)$ is beyond our work.

3.4.3 Variation of peak altitudes

The altitudes of the peak values of $O_2(^1\Sigma)$ and $O_2(^1\Delta)$ are shown in Fig. 8c and d. The altitudes of the peak values of $O_2(^1\Sigma)$ roughly follow the maximum intensity of solar radiance but show highest values at low-to-middle latitudes. We refer to the maximum intensity of solar radiance as the latitudes and times in which solar zenith angles have their lowest values. The low values of the maximum VERs and the high altitudes of the maximal VERs at the outermost high latitudes in the northern winters correspond to low signal-to-noise ratios and are below our significance level.

In the regions where the secondary maxima of O₂(¹Δ) happen, the peak altitudes occur in the ~84–89 km altitude range.

3.4.4 Centroid altitudes

The estimation of the peak altitude is affected by instrument noise and vertical resolution. A more stable measure is the centroid altitude h_{CA} :

$$h_{CA} = \frac{\sum_i a_i v_i}{\sum_i v_i}, \quad (6)$$

where v_i is the volume emission rate at altitude a_i , which ranges from ~50 to ~150 km for O₂(¹Σ) and from ~85 to ~100 km for O₂(¹Δ). Figure 8e shows the centroid altitude for daytime O₂(¹Σ) and Fig. 8f for daytime O₂(¹Δ).

The maximum h_{CA} values of the O₂(¹Σ) band are correlated with the (maximum intensity) of solar radiance. We also observe maximal values of h_{CA} in a narrow band at northern polar latitudes, where the solar flux generally is low. This also suggests recombination of atomic oxygen as a source, as discussed in the Sect. 3.4.2. The very low values of the h_{CA} s, at the highest latitudes, mostly in the hemispheric wintertimes, correspond to low signal-to-noise ratios of the corresponding VERs (not shown here) and are below our significance level.

The O₂(¹Δ) secondary maximums occur in winter at high latitudes. The values of the O₂(¹Δ) h_{CA} range between ~88 and ~89 km altitude.

Figure 8c, d, and f show a decrease in the altitude of the maximum O₂(¹Σ), altitude of the maximum O₂(¹Δ), and O₂(¹Δ) h_{CA} respectively between November 2010 and February 2011. This is due to a change in the limb sequence so that tangent altitudes were shifted, as seen for example at lower altitudes in these days. However, this does not have any notable effect on the VER time series in Figs. 7a, b, 8a, and b.

3.4.5 Discussion of temporal–spatial variation

The temporal–latitudinal variation in peak values and altitudes suggests that O₂(¹Σ) at 85–100 km altitude is formed by a combination of ozone photolysis and atomic oxygen recombination. At high latitudes during winter and spring, atomic oxygen recombination dominates, but, in the subsolar region, ozone photolysis is more important. In contrast, the secondary peak of O₂(¹Δ) stems mainly from atomic oxygen recombination, in particular at high latitudes during winter.

The temporal–latitudinal variation in peak values and altitudes suggests that the daytime VERs of O₂(¹Δ) and O₂(¹Σ) in the altitude range of 80–100 km are formed by a combination of ozone and O₂ photolysis and atomic oxygen recombination. At high latitudes during winter and spring, atomic oxygen recombination dominates, but, in the subpolar region, photolysis of ozone and O₂ is more important.

To test whether these conclusions are generally consistent with our understanding of the photochemical production and loss of O₂(¹Δ) and O₂(¹Σ), a simple photochemical model covering the production and loss reactions summarized in Sect. 1 (Reactions R1–R15) was set up. Photochemical equilibrium was considered for O₂(*c*¹Σ_u[−]), O(¹S), O(¹D), O₂(¹Δ), and O₂(¹Σ). Reaction rates were taken from the JPL recommendation (Burkholder et al., 2015) with the exception of the quenching of the intermediate O₂(*c*¹Σ_u[−]) state (the q_6 and q_7 rates shown in Fig. 1), which was taken from Stegman and Murtagh (1991) with δ coefficients from Bates (1988). Einstein coefficients for the O₂(¹Σ) → O₂(*X*³Σ_g[−]) transition (A_2 in Fig. 1) were taken from Mlynczak and Solomon (1993), for the O(¹S) → O(¹D) transition (A_4 in Fig. 1) from the NIST atomic spectra database ², for the O(¹S) → O(³P) transition (A_5 in Fig. 1) from the NIST atomic spectra database, and for the O₂^{*} products (not given in Fig. 1) from Stegman and Murtagh (1991). Photolysis rates for solar zenith angles 0, 10, 20, 30, 40, 50, 60, 70, 80, and 88° were calculated using a fixed ozone profile using the 3dCTM model (Sinnhuber et al., 2012). The rate of photoexcitation of the ground state O₂(*X*³Σ_g[−]) to the second excited state O₂(¹Σ) was calculated following (Bucholtz et al., 1986) but using recent line-strength data provided by the HITRAN database at <http://hitran.org> (Rothman et al., 2013), yielding a rate of 2.04×10^{-9} photons cm^{−3} s^{−1} above 70 km. Temperature, total air density, and the densities of O₂ and N₂ were taken from the NRLMSISE-00 model (Picone et al., 2002) at 10:00 local time at the equator. The production of O(¹D) by photolysis of H₂O and CO₂ in the Ly- α range was also considered, and H₂O and CO₂ were assumed to have constant mixing ratios of 1 ppm (H₂O) and 380 ppm (CO₂). Ozone density was adapted from a multi-year global average of SABER data in the altitude region 70–104 km (see Smith et al., 2013, Fig. 3). Atomic oxygen was calculated from photochemical equilibrium of ozone considering only ozone photolysis and production by O + O₂. The resulting VERs of O₂(¹Δ) and O₂(¹Σ) are shown in Fig. 9, compared to the SCIAMACHY daytime data of 3 February 2010 (shown in Fig. 5). Considering that the ozone profile, O₂, N₂, and temperature are not chosen to fit those specific observations, the agreement is very good for both emissions, indicating that the main processes of O₂(¹Δ) and O₂(¹Σ) formation and loss are reproduced well by this simple model. Also shown are the contributions of the individual production reactions: O + O, quenching of O(¹D), and resonance excitation of O₂(*X*³Σ_g[−]) for O₂(¹Σ), O + O, quenching of O(¹Σ), and ozone photolysis for O₂(¹Δ).

Below about 82 km, O₂(¹Σ) is formed in about equal amounts by quenching of O(¹D), while above quenching of O(¹D) dominates. The reaction of O + O contributes about 1 order of magnitude less O₂(¹Σ) than the other two branches even in the region where it has the largest contribu-

²www.nist.gov

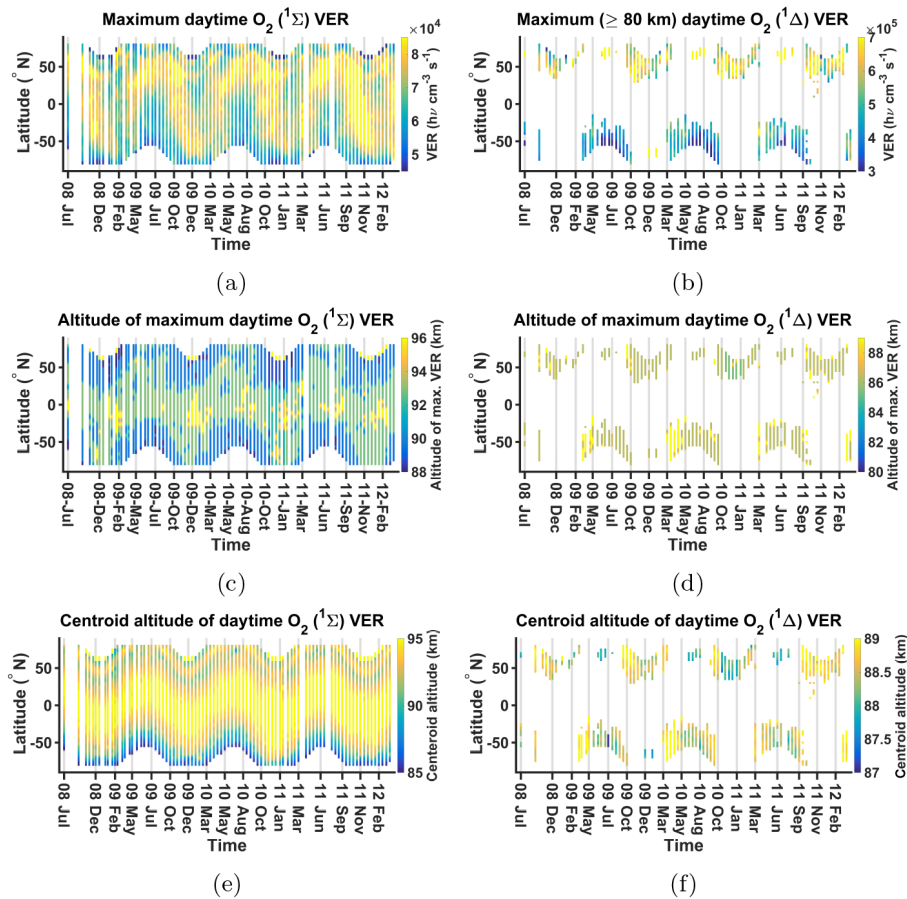


Figure 8. (a) Time series of the maximal daily mean $O_2(^1\Sigma)$ VER. (b) as (a) for the $O_2(^1\Delta)$ band. (c) Time series of the altitudes of the maximum daily mean $O_2(^1\Sigma)$ VER. (d) as (c) for the $O_2(^1\Delta)$ band. (e) Time series of the centroid altitudes of the daytime $O_2(^1\Sigma)$ daily mean VER (km). (f) as (e) for the $O_2(^1\Delta)$ band.

tion (around 90 km). This is consistent with the ratio of emission intensities during twilight and during daytime of about a factor of 10 as discussed in Sect. 3.1, considering that, during nighttime and twilight, $O_2(^1\Sigma)$ is formed solely by the $O + O$ reaction. The formation of $O_2(^1\Delta)$ is dominated by ozone photolysis at all altitudes, though below 90 km $O_2(^1\Sigma)$ quenching contributes about 10–25 %.

$O(^1D)$ is formed mainly by photolysis of O_3 below 90 km and by photolysis of O_2 above that altitude. During daytime, both the $O_2(^1\Delta)$ and $O_2(^1\Sigma)$ states are formed by photolysis in agreement with our observation that the peak maxima correlate with the maximum intensity of solar radiance. The contribution of the $O + O$ reaction generally is smaller by 1 to 3 orders of magnitude than the contribution of photolysis, in agreement with the lower VERs observed during twilight when photolysis is not a significant production process. However, it should be pointed out that the relation between the O_2 airglow and atomic oxygen by the $O + O$ reaction and de-excitation of the excited intermediate states such as $O_2(c^1\Sigma_u^-)$ is probably quadratic to cubic; increased amounts of atomic oxygen, e.g., at high latitudes during winter when

large amounts of atomic oxygen can be transported or mixed down from the lower thermosphere, can therefore increase the contribution of the $O + O$ reaction to the overall airglow considerably. This explains the observed enhancements of the airglow at high northern latitudes in winter and spring, in particular as the centroid altitudes in these occasions range around 90 km, the altitude where the $O + O$ reaction has the strongest influence.

3.5 Relationship between the VER time series variations and sudden stratospheric warmings – example

Sudden stratospheric warmings are dynamical phenomena in the winter polar stratosphere caused by upward propagating planetary waves interacting with the mean flow (Matsuno, 1971). During the so-called recovery phase of SSWs, the reformation of the jet changes gravity wave propagation to the mesosphere. The induced change in the residual circulation results in an enhanced descent of air. This causes adiabatic warming and the stratopause reforms at altitudes as high as

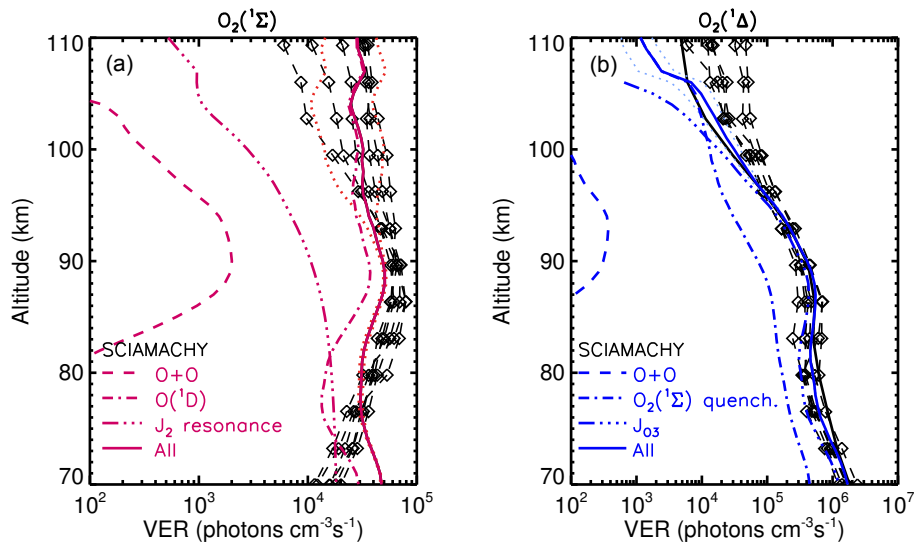


Figure 9. Modeled VERs of $O_2(^1\Sigma)$ (a) and $O_2(^1\Delta)$ (b). Solid lines are the mean of all model results for solar zenith angles 0, 10, 20, 30, 40, 50, 60, 70, 80, and 88° considering all formation processes; dotted lines show the variability due to photolysis reactions (\pm standard deviation). The dashed, dash-dotted, and dash-dot-dot lines show the contributions of individual formation processes: O + O, O(1D) quenching, and resonant excitation for $O_2(^1\Sigma)$, O + O, $O_2(^1\Sigma)$, and ozone photolysis for $O_2(^1\Delta)$. Black lines with symbols are SCIAMACHY profiles at five latitudes observed on 3 February 2010 (see Fig. 5).

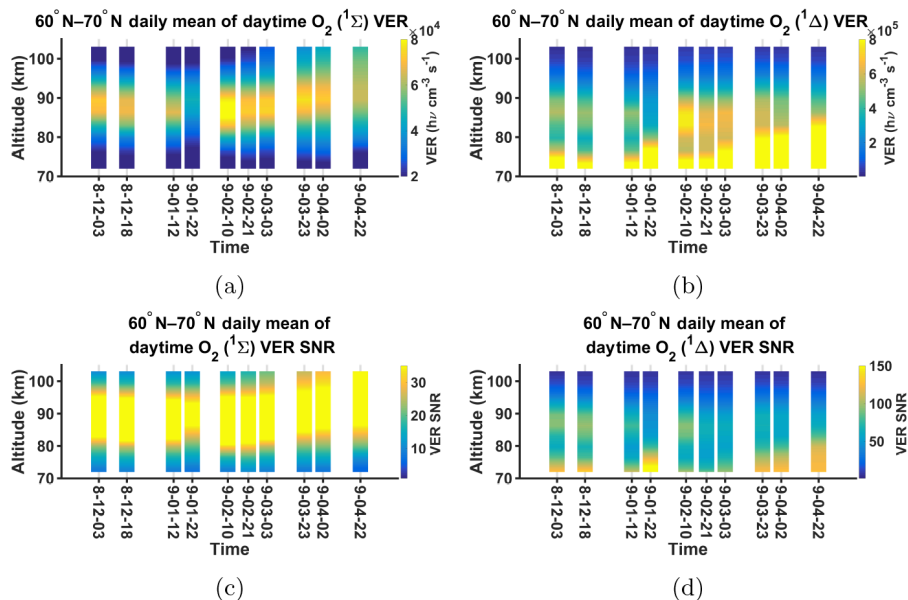


Figure 10. (a) Daily mean of the daytime $O_2(^1\Sigma)$ VER from December 2008 to April 2009 averaged between 60 and 70° N latitude. (b) as (a) for the $O_2(^1\Delta)$ band. (c) Daily mean of the signal-to-noise ratios of the daytime $O_2(^1\Sigma)$ VER from December 2008 to April 2009 averaged between 60 and 70° N latitude. (d) as (c) for $O_2(^1\Delta)$ VER signal-to-noise ratios.

75–80 km (Siskind et al., 2010). The unusual brightening of the OH airglow (Winick et al., 2009) is presumably caused by enhanced downwelling of atomic oxygen. According to Harada et al. (2010), a major SSW event happened around 21 January 2009 (Fig. 1 of that paper). We therefore expect to observe enhanced airglow at the end of January 2009.

Based on the temporal evolution of mesospheric temperature during the SSW event, Gao et al. (2011b) divided the response in the mesosphere into three stages: the period prior to day 15 is considered the normal stage, days 15–22 correspond to the cooling stage, and days post-22 correspond to the recovery stage. According to this, they reported that the

O_2 nightglow brightness decreased by about a factor of 10 during the cooling stage and then increased by about a factor of 3 during the recovery stage relative to the normal stage. Figure 10a and b show the time series from December 2008 to April 2009 of the daytime $O_2(^1\Sigma)$ and $O_2(^1\Delta)$ daily mean VER, averaged from 60 to 70° N. We observe that on the last day of the cooling stage, i.e., 22 January 2009, the daily zonal mean $O_2(^1\Sigma)$ and $O_2(^1\Delta)$ VERs show a reduced maximum intensity in the 82–87 km altitude range. We observe larger intensities on the next measurement day of SCIAMACHY about 3 weeks later, i.e., on 10 February 2009. This is expected from a decrease of atomic oxygen due to horizontal mixing and upwelling during the cooling stage and then downward extension of the MLT region with large mixing ratio of O during the recovery stage of the SSW (Gao et al., 2011b). On the measurement day of SCIAMACHY after the recovery phase, i.e., 23 March 2009, the relative difference in the $O_2(^1\Delta)$ signal is less prominent compared to the relative difference in $O_2(^1\Sigma)$. A detailed analysis of this relationship is beyond the scope of this paper.

We also note that the signal-to-noise ratios of the VERs for $O_2(^1\Sigma)$ shown in Fig. 10c are statistically significant. It is shown in Fig. 10d that, during and after the initial stage of the SSW event, the $O_2(^1\Delta)$ signal becomes weaker and stronger respectively, and the signal-to-noise ratio of the data are such that this behavior is statistically significant.

4 Discussion and conclusions

We present the retrieval of daytime and twilight $O_2(^1\Sigma)$ and $O_2(^1\Delta)$ spectral emissions from MLT measurements of the airglow in limb-viewing geometry from the SCIAMACHY instrument onboard Envisat. From the retrieved spectra, we calculate the band integrated VERs for both bands. The maxima of the $O_2(^1\Sigma)$ VER and the centroid altitude of the $O_2(^1\Sigma)$ are correlated with the maximum intensity of solar radiance. High values of maximum VER and centroid altitude are additionally seen at northern polar latitudes. The (30° N) time series of $O_2(^1\Sigma)$ VER shows a maximum in the 90–98 km altitude range. The maximum values correspond to high centroid altitudes for $O_2(^1\Sigma)$. The daily zonal (60–70° N) mean $O_2(^1\Sigma)$ VERs show a reduced maximum intensity in the 82–87 km range and in the initiation of the sudden stratospheric warming 2009 event as well as an increase in intensity about 3 weeks later.

The maxima of the $O_2(^1\Delta)$ VERs are also correlated with the maximum intensity of solar radiance. They are most prominent in summer, while the altitudes of the maximal values have their highest values in winter, and both occur at high latitudes. The time series of $O_2(^1\Delta)$ VER is 2 orders of magnitude larger than $O_2(^1\Sigma)$ VER at its maximal values which are located below the observation altitude (< 60 km), but it shows some secondary maxima about 1 order of magnitude smaller than the primary maxima at 84–89 km. This happens

in winter at high latitudes. The maximum VERs correspond to the low centroid altitudes for the $O_2(^1\Delta)$ band. The daily zonal (60–70° N) mean $O_2(^1\Delta)$ VERs show a reduced maximum intensity in the 82–87 km range and in the initiation of the sudden stratospheric warming 2009 event as well as an increase in intensity about 3 weeks later, although the relative difference in the $O_2(^1\Delta)$ band signal is less prominent compared to the relative difference in $O_2(^1\Sigma)$.

The intensification of the VER during the sudden stratospheric warming in early 2009 presumably corresponds to the downwelling of the atomic oxygen following the warming, while the decrease is probably due to upwelling as well as horizontal mixing during the warming event.

Our results suggest that at low and middle latitudes $O_2(^1\Sigma)$ and $O_2(^1\Delta)$ abundances during daytime are dominated by photolysis of ozone below 90 km and by photolysis of ozone and O_2 above 90 km as supported by our observed correlation with solar illumination, and they are consistent with the processes depicted in Fig. 1. At high latitudes, however, in particular during winter, atomic oxygen abundances might be a more important driver due to the recombination of $O + O$ and subsequent de-excitation via $O(^1S)$ and $O_2(^1\Sigma)$.

As the formation of the $O_2(^1\Delta)$ band is dominated by ozone photolysis, this band can be used to derive ozone densities directly. However, as quenching of $O_2(^1\Sigma)$ contributes about 10–25 % to the overall production in 70–90 km, the accuracy of this retrieval can be improved considerably when both lines are available. The $O_2(^1\Sigma)$ band is dominated by quenching of $O(^1D)$, and daytime $O(^1D)$ can be derived from observations of the $O_2(^1\Sigma)$ VER. However, below ~ 90 km, the resonant excitation from the ground state has to be taken into account as well. The rate used here based on new line-strength data from HITRAN is lower by about a factor of 2 compared to a similar estimate used for HRDI data as described in Marsh et al. (2002) and lower by about a factor of 4 compared to the original estimate by Bucholtz et al. (1986). We conclude that the retrieval of $O(^1D)$ and ozone as the main source of $O(^1D)$ below 90 km from $O_2(^1\Sigma)$ is possible but needs a careful estimation of the rate of resonant excitation.

Data availability. The data are available on request to the authors (amirmahdi.zarboo@kit.edu or miriam.sinnhuber@kit.edu).

Competing interests. The authors declare that they have no conflict of interest.

Acknowledgements. Amirmahdi Zarboo and Miriam Sinnhuber gratefully acknowledge funding by BMBF grant 01LG1208A (ROMIC-MesoEnergy). The support of the BMBF ROMIC project for the University of Bremen is also gratefully acknowledged. The SCIAMACHY project was funded by Germany with support from

the Netherlands and Belgium as a national contribution to ESA Envisat. The authors also acknowledge the reviewers for the very constructive comments on the paper.

The article processing charges for this open-access publication were covered by a Research Centre of the Helmholtz Association.

Edited by: William Ward

Reviewed by: two anonymous referees

References

- Barth, C. A.: Three-body reactions, *Ann. Geophys.*, vol. 20, p. 182, 1964.
- Barth, C. A. and Hildebrandt, A. F.: The 5577 Å airglow emission mechanism, *J. Geophys. Res.*, 66, 985–986, 1961.
- Bates, D.: The green light of the night sky, *Planetary and Space Science*, 29, 1061–1067, [https://doi.org/10.1016/0032-0633\(81\)90003-9](https://doi.org/10.1016/0032-0633(81)90003-9), 1981.
- Bates, D.: Excitation and quenching of the oxygen bands in the nightglow, *Planet. Space Sci.*, 36, 875–881, 1988.
- Bates, D.: Nightglow emissions from oxygen in the lower thermosphere, *Planet. Space Sci.*, 40, 211–221, [https://doi.org/10.1016/0032-0633\(92\)90059-W](https://doi.org/10.1016/0032-0633(92)90059-W), 1992.
- Bovensmann, H., Burrows, J. P., Buchwitz, M., Frerick, J., Noël, S., Rozanov, V. V., Chance, K. V., and Goede, A. P. H.: SCIAMACHY: Mission Objectives and Measurement Modes, *J. Atmos. Sci.*, 56, 127–150, 1999.
- Brasseur, G. P. and Solomon, S.: *Aeronomy of the middle atmosphere: chemistry and physics of the stratosphere and mesosphere*, vol. 32, Springer Science & Business Media, 2006.
- Bucholtz, A., Skinner, W., Abreu, V. J., and Hays, P.: The dayglow of the O₂ atmospheric band system, *Planet. Space Sci.*, 34, 1031–1035, 1986.
- Burkholder, J., Sander, S., Abbatt, J., Barker, J., Huie, R., Kolb, C., Kurylo, M., Orkin, V., Wilmouth, D., and Wine, P.: *Chemical Kinetics and Photochemical Data for Use in Atmospheric Studies*, Evaluation Number 18, NASA panel for data evaluation technical report, 2015.
- Burrows, J. P., Hölzle, E., Goede, A. P. H., Visser, H., and Fricke, W.: SCIAMACHY–scanning imaging absorption spectrometer for atmospheric cartography, *Acta Astronaut.*, 35, 445–451, [https://doi.org/10.1016/0094-5765\(94\)00278-T](https://doi.org/10.1016/0094-5765(94)00278-T), 1995.
- Christensen, A. B., Yee, J.-H., Bishop, R. L., Budzien, S. A., Hecht, J. H., Sivjee, G., and Stephan, A. W.: Observations of molecular oxygen Atmospheric band emission in the thermosphere using the near infrared spectrometer on the ISS/RAIDS experiment, *J. Geophys. Res.-Space*, 117, A04315, <https://doi.org/10.1029/2011JA016838>, 2012.
- DeMore, W. B.: Primary Processes in Ozone Photolysis, *J. Chem. Phys.*, 44, 1780, <https://doi.org/10.1063/1.1726939>, 1966.
- Evans, W. F. J., Hunten, D. M., Llewellyn, E. J., and Jones, A. V.: Altitude profile of the infrared atmospheric system of oxygen in the dayglow, *J. Geophys. Res.*, 73, 2885–2896, <https://doi.org/10.1029/JA073i009p02885>, 1968.
- Gao, H., Xu, J., Chen, G., Yuan, W., and Beletsky, A. B.: Global distributions of OH and O₂ (1.27 μm) nightglow emissions observed by TIMED satellite, *Sci. China Technol. Sc.*, 54, 447–456, <https://doi.org/10.1007/s11431-010-4236-5>, 2011a.
- Gao, H., Xu, J., Ward, W., and Smith, A. K.: Temporal evolution of nightglow emission responses to SSW events observed by TIMED/SABER, *J. Geophys. Res.-Atmos.*, 116, D19110, <https://doi.org/10.1029/2011JD015936>, 2011b.
- Greer, R., Llewellyn, E., Solheim, B., and Witt, G.: The excitation of O₂ (b¹Σ_g⁺) in the nightglow, *Planet. Space Sci.*, 29, 383–389, 1981.
- Harada, Y., Goto, A., Hasegawa, H., Fujikawa, N., Naoe, H., and Hirooka, T.: A Major Stratospheric Sudden Warming Event in January 2009, *J. Atmos. Sci.*, 67, 2052–2069, <https://doi.org/10.1175/2009JAS3320.1>, 2010.
- Hays, P. B., Abreu, V. J., Dobbs, M. E., Gell, D. A., Grassl, H. J., and Skinner, W. R.: The high-resolution doppler imager on the Upper Atmosphere Research Satellite, *J. Geophys. Res.*, 98, 10713–10723, <https://doi.org/10.1029/93JD00409>, 1993.
- Huestis, D. L.: *Current Laboratory Experiments for Planetary Aeronomy*, American Geophysical Union, 245–258, <https://doi.org/10.1029/130GM16>, 2013.
- Khomich, V. Y., Semenov, A. I., and Shefov, N. N.: *Airglow as an indicator of upper atmospheric structure and dynamics*, Springer, <https://doi.org/10.1007/978-3-540-75833-4>, 2008.
- Killeen, T. L., Wu, Q., Solomon, S. C., Ortland, D. A., Skinner, W. R., Niciejewski, R. J., and Gell, D. A.: TIMED Doppler Interferometer: Overview and recent results, *J. Geophys. Res.*, 111, A10S01, <https://doi.org/10.1029/2005JA011484>, 2006.
- Kirilov, A.: The calculation of quenching rate coefficients of O₂ Herzberg states in collisions with CO₂, CO, N₂, O₂ molecules, *Chem. Phys. Lett.*, 592, 103–108, <https://doi.org/10.1016/j.cplett.2013.12.009>, 2014.
- Kirilov, A. S.: Model of vibrational level populations of Herzberg states of oxygen molecules at heights of the lower thermosphere and mesosphere, *Geomagn. Aeronomy+*, 52, 242–247, <https://doi.org/10.1134/S0016793212020077>, 2012.
- Kurnosova, L., Kolobyanina, T., Logachev, V., Razorenov, L., Sirotkin, I., and Fradkin, M.: Discovery of radiation anomalies above the South Atlantic at heights of 310–340 km, *Planet. Space Sci.*, 9, 513–516, [https://doi.org/10.1016/0032-0633\(62\)90057-0](https://doi.org/10.1016/0032-0633(62)90057-0), 1962.
- Lednyts'kyi, O., von Savigny, C., Eichmann, K.-U., and Mlynczak, M. G.: Atomic oxygen retrievals in the MLT region from SCIAMACHY nightglow limb measurements, *Atmos. Meas. Tech.*, 8, 1021–1041, <https://doi.org/10.5194/amt-8-1021-2015>, 2015.
- Llewellyn, E. J., Lloyd, N. D., Degenstein, D. A., Gattinger, R. L., Petelina, S. V., Bourassa, A. E., Wiensz, J. T., Ivanov, E. V., McDade, I. C., Solheim, B. H., McConnell, J. C., Haley, C. S., von Savigny, C., Sioris, C. E., McLinden, C. A., Griffioen, E., Kaminski, J., Evans, W. F., Puckrin, E., Strong, K., Wehrle, V., Hum, R. H., Kendall, D. J., Matsushita, J., Murtagh, D. P., Brohede, S., Stegman, J., Witt, G., Barnes, G., Payne, W. F., Piché, L., Smith, K., Warshaw, G., Deslauniers, D. L., Marchand, P., Richardson, E. H., King, R. A., Wevers, I., McCreath, W., Kyrölä, E., Oikarinen, L., Leppelmeier, G. W., Auvinen, H., Mégie, G., Hauchecorne, A., Lefèvre, F., de La Nöe, J., Ricaud, P., Frisk, U., Sjöberg, F., von Schéele, F., and Nordh, L.: The OSIRIS instrument on the Odin spacecraft, *Can. J. Phys.*, 82, 411–422, <https://doi.org/10.1139/p04-005>, 2004.

- Marsh, D. R., Skinner, W. R., Marshall, A. R., Hays, P. B., Orland, D. A., and Yee, J.-H.: High Resolution Doppler Imager observations of ozone in the mesosphere and lower thermosphere, *J. Geophys. Res.-Atmos.*, 107, 4390, <https://doi.org/10.1029/2001JD001505>, 2002.
- Matsuno, T.: A dynamical model of the stratospheric sudden warming, 28, 1479–1494, [https://doi.org/10.1175/1520-0469\(1971\)028<1479:ADMOTS>2.0.CO;2](https://doi.org/10.1175/1520-0469(1971)028<1479:ADMOTS>2.0.CO;2), 1971.
- Mlynczak, M., Morgan, F., Yee, J.-H., Espy, P., Murtagh, D., Marshall, B., and Schmidlin, F.: Simultaneous measurements of the O₂(¹Δ) and O₂(¹Σ) Airglows and ozone in the daytime mesosphere, *Geophys. Res. Lett.*, 28, 999–1002, 2001.
- Mlynczak, M. G. and Olander, D. S.: On the utility of the molecular oxygen dayglow emissions as proxies for middle atmospheric ozone, *Geophys. Res. Lett.*, 22, 1377–1380, <https://doi.org/10.1029/95GL01321>, 1995.
- Mlynczak, M. G. and Solomon, S.: A detailed evaluation of the heating efficiency in the middle atmosphere, *J. Geophys. Res.-Atmos.*, 98, 10517–10541, 1993.
- Mlynczak, M. G., Solomon, S., and Zaras, D. S.: An updated model for O₂(¹Δ_g) concentrations in the mesosphere and lower thermosphere and implications for remote sensing of ozone at 1.27 μm, *J. Geophys. Res.-Atmos.*, 98, 18639–18648, <https://doi.org/10.1029/93JD01478>, 1993.
- Mlynczak, M. G., Marshall, B. T., Martin-Torres, F. J., Russell, J. M., Thompson, R. E., Remsberg, E. E., and Gordley, L. L.: Sounding of the Atmosphere using Broadband Emission Radiometry observations of daytime mesospheric O₂(¹Δ) 1.27 μm emission and derivation of ozone, atomic oxygen, and solar and chemical energy deposition rates, *J. Geophys. Res.-Atmos.*, 112, D15306, <https://doi.org/10.1029/2006JD008355>, 2007.
- Nicolet, M.: Aeronomic reactions of hydrogen and ozone, in: *Mesospheric models and related experiments*, Springer, 1–51, 1971.
- Picone, J., Hedin, A., Drob, D. P., and Aikin, A.: NRLMSISE-00 empirical model of the atmosphere: Statistical comparisons and scientific issues, *J. Geophys. Res.-Space*, 107, 1468, <https://doi.org/10.1029/2002JA009430>, 2002.
- Rothman, L., Gordon, I. E., Babikov, Y., Barbe, A., Benner, D. C., Bernath, P. F., Birk, M., Bizzocchi, L., Boudon, V., Brown, L. R., Campargue, A., Chance, K., Cohen, E. A., Coudert, L. H., Devi, V. M., Drouin, B. J., Fayt, A., Flaud, J.-M., Gamache, R. R., Harrison, J. J., Hartmann, J.-M., Hill, C., Hodges, J. T., Jacquemart, D., Jolly, A., Lamouroux, J., Le Roy, R. J., Li, G., Long, D. A., Lyulin, O. M., Mackie, C. J., Massie, S. T., Mikhailenko, S., Müller, H. S. P., Naumenko, O. V., Nikitin, A. V., Orphal, J., Perevalov, V., Perrin, A., Polovtseva, E. R., Richard, C., Smith, M. A. H., Starikova, E., Sung, K., Tashkun, S., Tennyson, J., Toon, G. C., Tyuterev, V. I., and Wagner, G.: The HITRAN 2012 Molecular Spectroscopic Database, *J. Quant. Spectrosc. Ra.*, 130, 4–50, <https://doi.org/10.1016/j.jqsrt.2013.07.002>, 2013.
- Sheese, P. E., Llewellyn, E. J., Gattinger, R. L., Bourassa, A. E., Deegenstein, D. A., Lloyd, N. D., and McDade, I. C.: Temperatures in the upper mesosphere and lower thermosphere from OSIRIS observations of O₂ A-band emission spectra, *Can. J. Phys.*, 88, 919–925, <https://doi.org/10.1139/P10-093>, 2010.
- Shepherd, G. G., Thuillier, G., Gault, W. A., Solheim, B. H., Hersom, C., Alunni, J. M., Brun, J.-F., Brune, S., Charlot, P., Cogger, L. L., Desaulniers, D.-L., Evans, W. F. J., Gattinger, R. L., Girod, F., Harvie, D., Hum, R. H., Kendall, D. J. W., Llewellyn, E. J., Lowe, R. P., Ohrt, J., Pasternak, F., Peillet, O., Powell, I., Rochon, Y., Ward, W. E., Wiens, R. H., and Wimperis, J.: WINDII, the wind imaging interferometer on the Upper Atmosphere Research Satellite, *J. Geophys. Res.*, 98, 10725–10750, <https://doi.org/10.1029/93JD00227>, 1993.
- Sinnhuber, M., Nieder, H., and Wieters, N.: Energetic particle precipitation and the chemistry of the mesosphere/lower thermosphere, *Surv. Geophys.*, 33, 1281–1334, 2012.
- Siskind, D. E., Eckermann, S. D., McCormack, J. P., Coy, L., Hoppel, K. W., and Baker, N. L.: Case studies of the mesospheric response to recent minor, major, and extended stratospheric warmings, *J. Geophys. Res.-Atmos.*, 115, D00N03, <https://doi.org/10.1029/2010JD014114>, 2010.
- Skinner, W. and Hays, P.: Brightness of the O₂ atmospheric bands in the daytime thermosphere, *Planet. Space Sci.*, 33, 17–22, [https://doi.org/10.1016/0032-0633\(85\)90138-2](https://doi.org/10.1016/0032-0633(85)90138-2), 1985.
- Slanger, T., Cosby, P., Sharpee, B., Minschwaner, K., and Siskind, D.: O(¹S → ¹D, ³P) branching ratio as measured in the terrestrial nightglow, *J. Geophys. Res.-Space*, 111, A12318, <https://doi.org/10.1029/2006JA011972>, 2006.
- Slanger, T. G. and Copeland, R. A.: Energetic Oxygen in the Upper Atmosphere and the Laboratory, *Chem. Rev.*, 103, 4731–4765, <https://doi.org/10.1021/cr0205311>, 2003.
- Smith, A., Harvey, V., Mlynczak, M. G., Funke, B., García-Comas, M., Hervig, M., Kaufmann, M., Kyrölä, E., López-Puertas, M., McDade, I., Randall, C. E., Russell, J. M., Sheese, P. E., Shiotani, M., Skinner, W. R., Suzuki, M., and Walker, K. A.: Satellite observations of ozone in the upper mesosphere, *J. Geophys. Res.-Atmos.*, 118, 5803–5821, 2013.
- Smith, I. W. M.: The role of electronically excited states in recombination reactions, *Int. J. Chem. Kinet.*, 16, 423–443, <https://doi.org/10.1002/kin.550160411>, 1984.
- Stegman, J. and Murtagh, D.: The molecular oxygen band systems in the UV nightglow: measured and modelled, *Planet. Space Sci.*, 39, 595–609, 1991.
- Thomas, R. J., Barth, C. A., Rottman, G. J., Rusch, D. W., Mount, G. H., Lawrence, G. M., Sanders, R. W., Thomas, G. E., and Clemens, L. E.: Ozone density distribution in the mesosphere (50–90 km) measured by the SME limb scanning near infrared spectrometer, *Geophys. Res. Lett.*, 10, 245–248, <https://doi.org/10.1029/GL010i004p00245>, 1983.
- Thomas, R. J., Barth, C. A., Rusch, D. W., and Sanders, R. W.: Solar Mesosphere Explorer Near-Infrared Spectrometer: Measurements of 1.27-μm radiances and the inference of mesospheric ozone, *J. Geophys. Res.-Atmos.*, 89, 9569–9580, 1984.
- Wayne, R. P.: Singlet oxygen in the environmental sciences, *Res. Chem. Intermediat.*, 20, 395–422, <https://doi.org/10.1163/156856794X00397>, 1994.
- Winick, J., Wintersteiner, P., Picard, R., Esplin, D., Mlynczak, M., Russell, J., and Gordley, L.: OH layer characteristics during unusual boreal winters of 2004 and 2006, *J. Geophys. Res.-Space*, 114, A02303, <https://doi.org/10.1029/2008JA013688>, 2009.
- Wraight, P.: Association of atomic oxygen and airglow excitation mechanisms, *Planet. Space Sci.*, 30, 251–259, [https://doi.org/10.1016/0032-0633\(82\)90003-4](https://doi.org/10.1016/0032-0633(82)90003-4), 1982.
- Yamamoto, H., Makino, T., Sekiguchi, H., and Naito, I.: Infrared atmospheric band airglow radiometer on board the satellite OHZORA, *J. Geomagn. Geoelectr.*, 40, 321–333, 1988.